Supporting Information

Constructing a dual-protection heterointerface for durable anion exchange membrane seawater electrolysis at ampere-level current density

Yue Xu, [a] Yingjian He, [a] Shuaidong Li, [a] Shanling Li, [b] Junqin Shi, *[b] Zeyun Cai, *[c] Xi Lin, *[a] and Kailong Hu,*[ad]

[a] School of Materials Science and Engineering, and Institute of Materials Genome & Big Data, Harbin Institute of Technology, Shenzhen 518055, P. R. China

[b] State Key Laboratory of Solidification Processing, Center of Advanced Lubrication and Seal Materials, School of Materials Science and Engineering, Northwestern Polytechnical University, Xi'an, Shanxi 710072, P. R. China.

[c] Institute of Special Environments Physical Sciences, Harbin Institute of Technology, Shenzhen 518055, P. R. China.

[d] Shenzhen Key Laboratory of New Materials Technology, Harbin Institute of Technology, Shenzhen 518055, Guangdong, P. R. China

Corresponding Author

*E-mail: hukailong@hit.edu.cn

*E-mail: linxi@hit.edu.cn

*E-mail: caizeyun@hit.edu.cn

*E-mail: junqin.shi@nwpu.edu.cn

Experimental section

Chemicals. Nickel chloride hexahydrate ($NiCl_2 \cdot 6H_2O$, 99% purity, Macklin Inc.), sodium molybdate dihydrate ($Na_2MoO_4 \cdot 2H_2O$, 99% purity, Macklin Inc.), sodium chloride (NaCl, 99.5% purity, Macklin Inc.), magnesium chloride hexahydrate ($MgCl_2 \cdot 6H_2O$, 98% purity, Macklin Inc.), magnesium sulfate heptahydrate ($MgSO_4 \cdot 7H_2O$, 99% purity, Macklin Inc.), calcium chloride hexahydrate ($CaCl_2 \cdot 6H_2O$, 97% purity, Macklin Inc.), sodium bicarbonate ($NaHCO_3$, 99.8% purity, Macklin Inc.), potassium chloride (KCl, 99.5% purity, Macklin Inc.), platinum nominally 20% on carbon black (20% Pt/C, Macklin Inc.), benzene (C_6H_6, 99.5% purity, Macklin Inc.), pyridine (C_5H_5N, 99.5% purity, Xilong Scientific Co., Ltd), Nafion (5 wt%, D520, Dupont de Nemours, Inc.) were used without further purification. Ultrapure water (18 $M\Omega\ cm^{-1}$) was used to prepare all aqueous solutions and wash samples.

Synthesis of NiMo sample. The $NiMoO_4$ precursor was synthesized through a standard hydrothermal method. 5 mmol of $NiCl_2 \cdot 6H_2O$ (99% purity, Macklin Inc.) and 5 mmol of $Na_2MoO_4 \cdot 2H_2O$ (99% purity, Macklin Inc.) were dissolved in 60 mL of ultrapure water. The mixture was transferred into a 100 mL Teflon-coated stainless autoclave, and maintained at 150 ºC for 12 h. After cooling the autoclave to room temperature, the as-prepared $NiMoO_4$ were washed multiple times with ultrapure water. Subsequently, the $NiMoO_4$ were dried overnight at 80 ºC in an oven. The dried $NiMoO_4$ powder was loaded onto a corundum boat and placed inside a quartz tube (φ50×φ47×1200 mm) within a furnace. The $NiMoO_4$ was reduced at 950 ºC for 20 min under the mixed

atmosphere of H_2 (200 sccm) and Ar (200 sccm) to form porous NiMo alloy[1].

Construction of G/NiMo and NG/NiMo heterointerface. Through annealing at 950 ºC for 20 min under a H_2/Ar mixed atmosphere, $NiMoO_4$ was reduced to form a porous NiMo alloy. Subsequently, the furnace temperature was lowered to 700 ºC for the growth of graphene on the surface of NiMo. The pure graphene and N-doped graphene were deposited on the as-obtained porous NiMo surface using method using benzene (C_6H_6, 99.5% purity, Macklin Inc.) and pyridine (C_5H_5N, 99.5% purity, Xilong Scientific Co., Ltd) as precursors via chemical vapor deposition (CVD). The deposition time of benzene and pyridine was controlled as 1.0 s to generate graphene layers. Cooling down to room temperature was achieved by employing a fan cooling system. The resulting samples were denoted as G/NiMo (pure graphene/NiMo alloy) and NG/NiMo (N-doped graphene/NiMo alloy).

Material characterizations. The microstructure and morphology of the samples was examined by scanning electron microscope (SEM, Phenom-Scientific Phenom Pro and Gemini SEM560), transmission electron microscopes (TEM, FEI Tecnai G2 F30), and equipped energy disperse spectroscopy (EDS). XRD analysis was conducted using the D2 PHASER (Haoyuan Instruments) with Cu Kα1 radiation. Raman spectra were acquired using a micro-Raman spectrometer (Renishaw InVia Reflex) operating at an incident wavelength of 532 nm. Fourier transform infrared (FTIR) spectra was obtained by utilizing an FTIR spectrometer (Nicolet iN10, Thermo Scientific). XPS analyses were performed on an X-ray photoelectron spectrometer (Thermo Scientific Nexsa) employing

an Al Kα radiation and X-ray monochromator.

Electrochemical measurements. Electrochemical measurements were performed using an electrochemical workstation (BioLogic, VSP-300) with a three-electrode system. The simulated seawater (26.86 g of NaCl, 4.94 g of $MgCl_2 \cdot 6H_2O$, 7.05 g of $MgSO_4 \cdot 7H_2O$, 2.28 g of $CaCl_2 \cdot 6H_2O$, 0.19 g of $NaHCO_3$, 0.72 g of KCl in 1.0 L of ultrapure water, pH≈8) was used as electrolyte. A graphite plate, an Ag/AgCl electrode equipped with double salt bridges, and the sample ink deposited carbon cloth served as the counter electrode, reference electrode, and working electrode, respectively. 5.0 mg of sample and 120 μL of Nafion (5 wt%, D520, Dupont de Nemours, Inc.) ware added in 480 μL of ethanol to prepare the sample ink after an ultrasonication for 30 min. The ink was dropped on a carbon cloth (1.0 cm × 1.0 cm, W0S1011, Cetech Co., Ltd.) and the catalyst loading amount was 5.0 mg. All potentials were calculated with respect to reversible hydrogen electrode (RHE) using the equation: E(RHE) = E(Ag|AgCl) + 0.0591 × pH + 0.197. Polarization curves were obtained under a sweep rate of 5.0 mV/s with 85% *iR* compensation. Electrochemical impedance spectroscopy (EIS) measurements were conducted over the frequency ranged from 100 kHz to 100 mHz under the potential of −0.5 V *vs*. RHE. The electric double layer capacitance (C_{dl}) was estimated by CV cycling measured at different sweep speeds from 10 to 100 mV/s under the potential between 0.2 and 0.3 V *vs*. RHE where no Faradaic process occurs. The ΔJ was calculated as $\Delta J = J_a - J_c$ at +0.25 V *vs*. RHE and the C_{dl} value was obtained by plotting half of the ΔJ against the sweep rates. CA tests were performed without *iR* compensation under the potential of

−0.6 V *vs*. RHE.

ICP testing. Samples and electrolyte adopted the same preparation method as electrochemical measurements section. The samples were subjected to a 1-h CA test under the potential of −0.6 V vs. RHE to achieve a stable test state. Then the solution was replaced with fresh simulated seawater after the activation reaction to ensure the removal of metal salt released on the surface. The post-reaction solution was filtered through filter membrane to eliminate solid components. ICP-MS instrument (NexION 1000, PerkinElmer) was employed for subsequent analysis.

AEM electrolyzer cell setup. The anion-exchange membrane (PiperION A60, thickness: 60 μm, Versogen) underwent sequential chemical activation through immersion in 1 M KOH solution at room temperature for 2 h. The membrane was soaked again in freshly prepared 1 M KOH solution at room temperature for 1 h to promote the bicarbonate-to-hydroxide conversion, thereby enhancing its conductive properties. Then the membrane was washed with ultrapure water until the pH achieved 7.0. The AEM electrolyzer comprised two Ti plates with a central area of 1.0 cm^2, four sets of bolts, two gaskets (each with a thickness of 250 μm), and the membrane-electrode assembly (MEA). The MEA fabrication integrated catalyst-coated substrate (CCS) and catalyst-coated membrane (CCM) methodologies. For cathode preparation, the catalysts were synthesized on Ti felt (thickness: 300 μm, area: 1.0 cm^2) and the as-prepared catalyst-loaded Ti felt was used as cathode diffusion layer. For anode preparation, the IrO_2 ink was obtained by mixing 2.0 mg of IrO_2 with 350 μL of isopropanol, 50 μL of ultrapure

water, and 2.0 μL of Nafion solution after an ultrasonication for 1 h. The resulted ink was subsequently sprayed onto the membrane to achieve a a loading of 2.5 mg cm^{-2}. The bare Ti felt was used as the anode diffusion layer. To ensure robust interfacial contact of MEA, the membrane was sandwiched between two Ti felt diffusion layers and compressed thermally at 1.0 MPa and 100°C for 2 minutes.

Cell testing. An electrochemical workstation (CS2350M, Wuhan Corrtest Instruments Co., Ltd.) was utilized to evaluate the performance and durablity of AEM electrolyzer. The AEM electrolyzer was firstly heated to 60°C, and the 0.5 M NaCl electrolyte was preheated to 70 °C and then pumped into the serpentine flow field on the anode side of electrolyzer at a flow rate of 6 mL min^{-1} via a peristaltic pump which ensured a stable water circulation at a constant temperature during the test. The polarization curves were measured at a scan rate of 10 mV s^{-1}, and the CP test was carried out at 1 A cm^{-2} at 60°C.

The activation energy calculation of metal dissolutions. The dissolution rate of samples during seawater reduction was determined by conducting weight-loss measurements within a temperature range of 25 to 60 ºC. Electrochemical measurements were performed under identical conditions as CA durability tests. The dissolution amounts of metals were calculated by measuring the concentration of specific metals that dissolved in the electrolyte at various time intervals. Inductively coupled plasma-mass spectrometry (ICP-MS, NexION 1000) was employed to quantify the metal concentration in the electrolyte. Dissolution rate values were estimated by plotting the dissolution

amount against time. The dissolution rate exhibited a temperature-dependent increase, consistent with the empirical Arrhenius equation:

$$r = A\ exp(-E_a/RT)\#(1)$$

where r represents the metal dissolution reaction rate, A represent the frequency factor, E_a represents the activation energy, R represents the absolute temperature, T represents the gas constant.

Exponential form of Arrhenius equation is denoted as:

$$\ln r = -E_a/RT + \ln A\#(2)$$

The activation energy of the metal dissolution reaction was obtained by plotting ln r against 1/T.

Molecular dynamics simulation. MD simulations were performed to study the ion distribution on bare NiMo alloy, graphene-coated NiMo alloy (G/NiMo), and N-doped graphene-coated NiMo alloy (NG/NiMo) surfaces. To reflect the solution concentration in experiments (that is 18969 mg/L for Cl^- ion), the solvent model was constructed, containing 15608 H_2O molecules, 150 Na^+, and 150 Cl^-. The sizes of model are about 79.63 Å × 72.92 Å × 81.88 Å, 79.57 Å × 76.74 Å × 91.86 Å, and 79.55 Å × 76.73 Å × 91.07 Å for NiMo, G/NiMo, and NG/NiMo substrate, respectively. In the last mode, 24 C atoms in the topmost graphene layer were replaced by N atoms, corresponding to the atomic ratio in XPS results. The interatomic interactions of three surfaces with H_2O and various ions were described by Coulomb and Lennard-Jones potentials, and the corresponding parameters of Na^+ and Cl^- were developed by Joung and Cheatham[2], as

listed in Table S1. The interaction of H_2O molecules was described by SPC/E model[3]. All the Leonard Jones parameters for each element were adopted from previous studies and force fields[3-6] (Table S1), and the Lorentz-Berthelot combining rule was used to calculate those parameters for any two elements. Periodic boundary conditions were applied in the horizonal directions. The three kinds of substrates were fixed to reduce the computational cost, and waters and ions are initially randomly distributed above the surface. In all simulations, each system was run at 300 K with NVT ensemble for 3 ns to reach equilibrium. The cutoff distance for Lennard-Jones potential was set to be 10.0 Å as an optimal balance between computation consumption and accuracy. The velocity Verlet algorithm was adopted to solve the equation of motions[7], and the timestep was set to be 1 fs. The MD simulations were implemented by using large-scale atomic/molecular massively parallel simulator (LAMMPS) code[8], and Ovito software was used for visual analysis of simulation results[9].

DFT calculations. DFT calculations were performed using the Vienna ab-initio simulation package (VASP)[10], employing the Perdew-Burke-Ernzerhof (PBE) functional within the generalized gradient approximation (GGA)[11] to describe exchange-correlation interactions. A plane-wave cutoff energy of 400 eV and a 3 × 3 × 1 k-point mesh were applied, with optimization of the unit cell until convergence criteria of 0.02 eV $Å^{-1}$ for force and 10^{-4} eV for total energy were achieved. The long-range weak van der Waals (vdW) interactions were corrected using the DFT-D3 method[12, 13]. Considering experimental challenges in characterizing the NiMo structure in a 1:1 ratio, we

hypothesized that it adopts the δ-phase NiMo: $Ni_{24}(Ni_4Mo_{16})Mo_{12}$ configuration[14], where the exposed surface is represented by the (100) plane. The reported lattice constant for NiMo (100) surface is 8.852 Å × 9.108 Å[14, 15], while the orthorhombic 2 × 4 graphene cell has a lattice constant of 8.52 Å × 9.838 Å. To address the lattice mismatch between graphene layer and NiMo (100) surface, a modified surface lattice constant of 8.852 Å × 9.563 Å was employed during calculations. With this adjusted lattice constant, N-doped graphene layers were positioned on the NiMo (100) surface. In addition, a vacuum region with a thickness of 20 Å was introduced between two neighbor slabs to prevent the interlayer interactions. The adsorption energy of Cl^- was evaluated using the following equation[16]:

$$M–O + Cl^- \rightarrow M–O–Cl + e^-$$

$$\Delta E(Cl^-) = E(M–Cl) – E(M–O) – 1/2E(Cl_2)$$

where M represents the catalytic active sites on the catalyst's surface. E(M–Cl), E(M–O), and $E(Cl_2)$ are the energies of Cl^- adsorbed on surface, the original surface, and single Cl_2 molecule, respectively.

Supporting figures

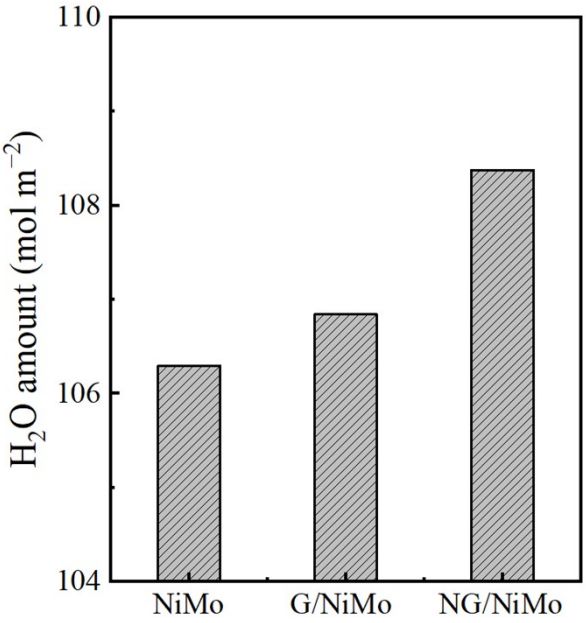

Figure S1. The MD-simulated quantities of H_2O molecules within 10 Å above the NiMo, G/NiMo, and NG/NiMo surfaces.

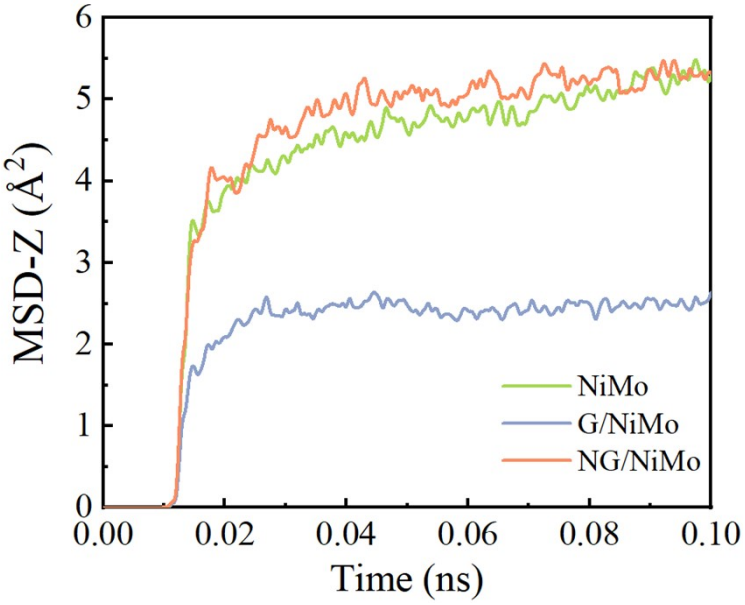

Figure S2. The mean square displacement in Z direction (MSD-Z) values of Cl^- ions on the NiMo, G/NiMo, and NG/NiMo surfaces.

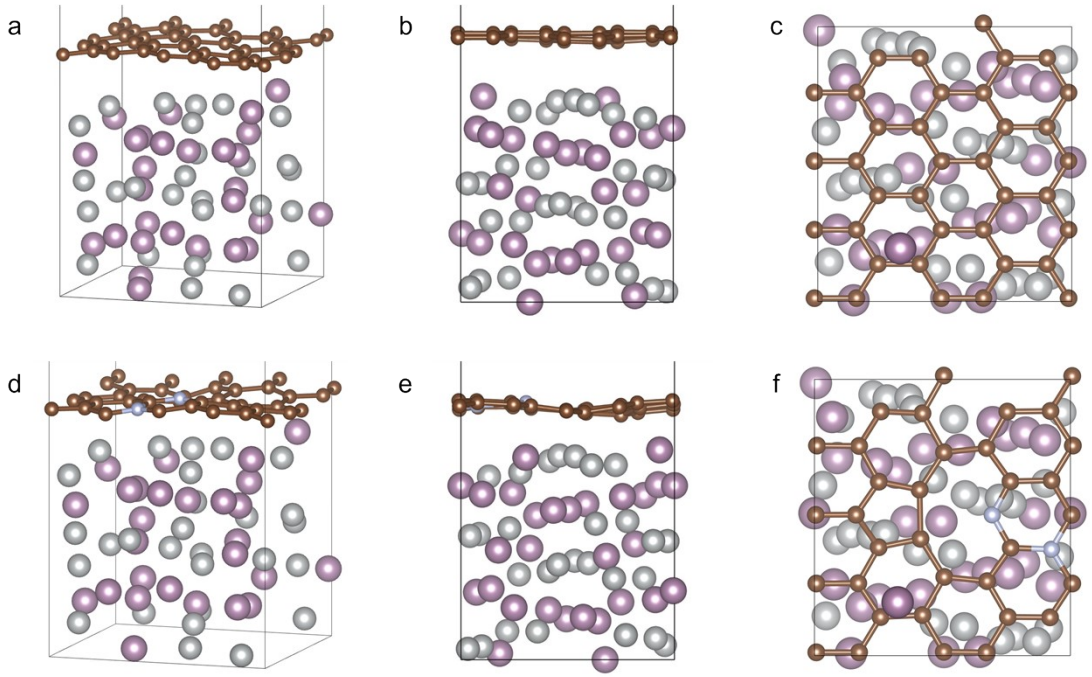

Figure S3. DFT models of (a-c) G/NiMo and (d-f) NG/NiMo. (a, d) Side views; (b, e) front views; and (c, f) top views.

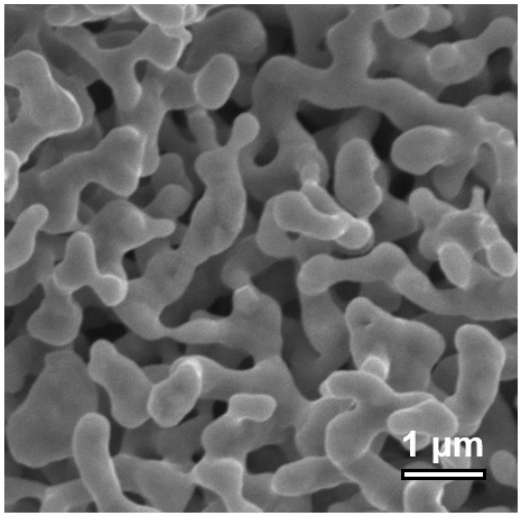

Figure S4. SEM image of NiMo sample.

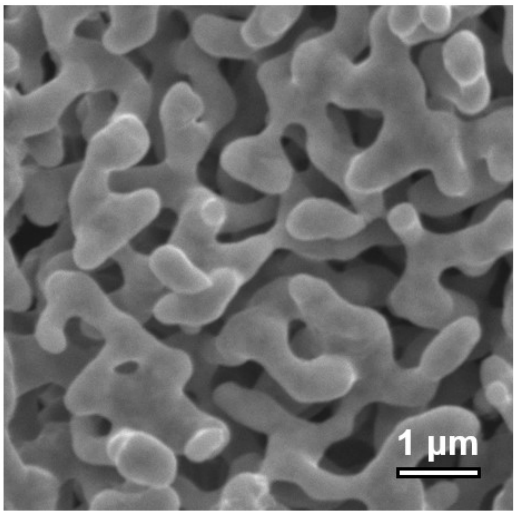

Figure S5. SEM image of G/NiMo sample.

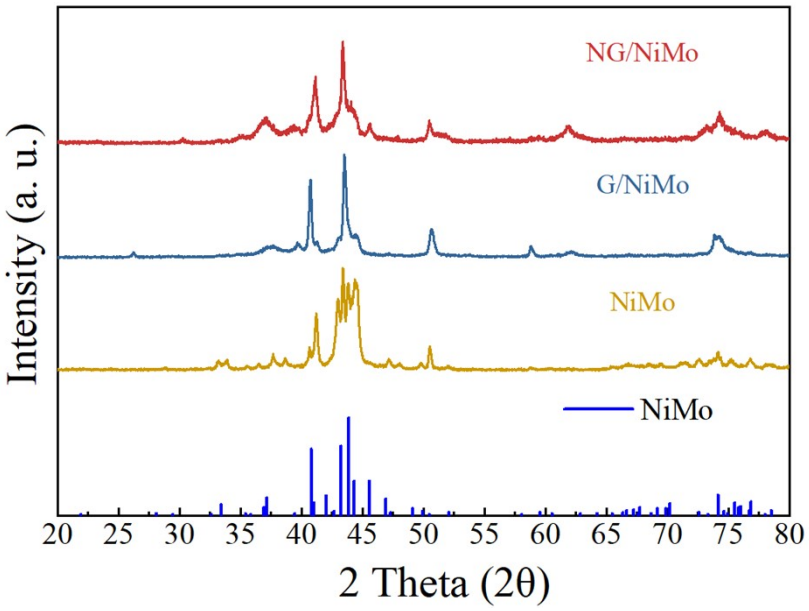

Figure S6. XRD patterns of NiMo, G/NiMo, and NG/NiMo samples.

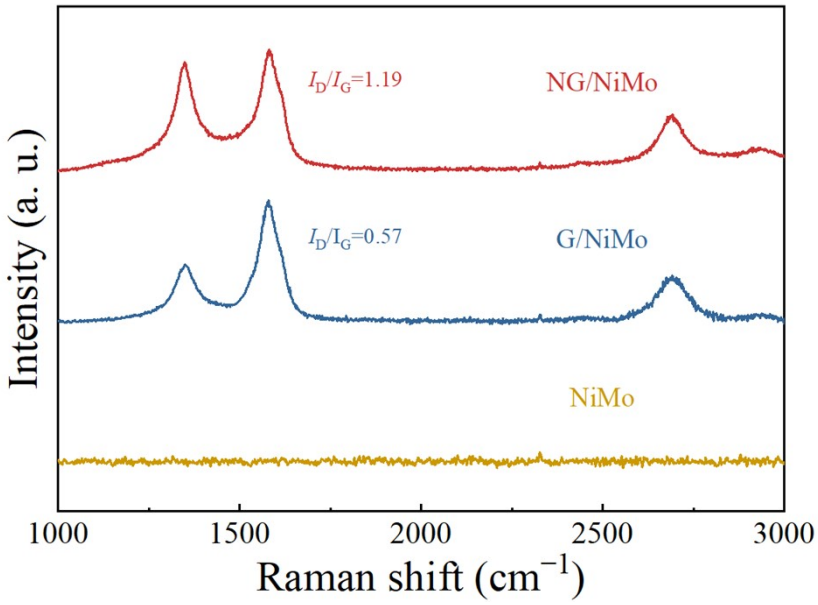

Figure S7. Raman spectra of NiMo, G/NiMo, and NG/NiMo samples.

The topological defects in G/NiMo are attributed to the curvature in porous NiMo surface.

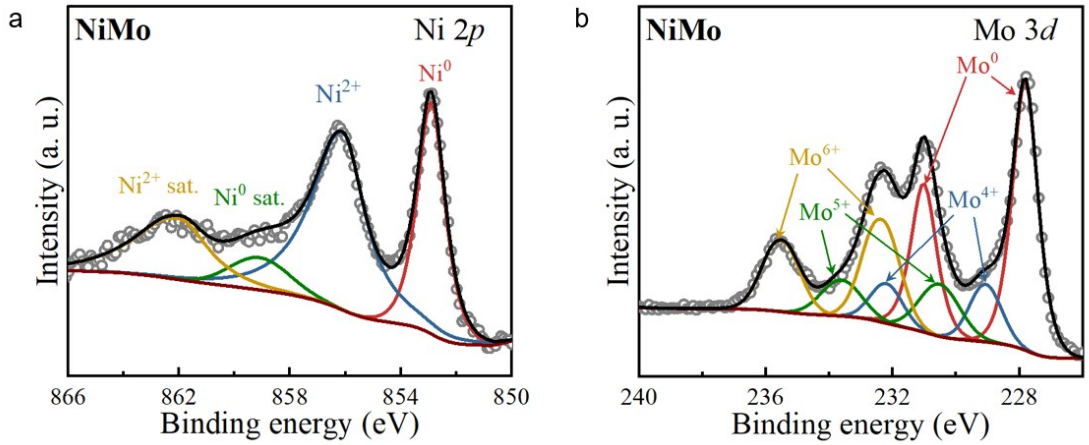

Figure S8. High-resolution XPS spectra of NiMo sample. (a) Ni 2*p* spectrum. (b) Mo 3*d* spectrum.

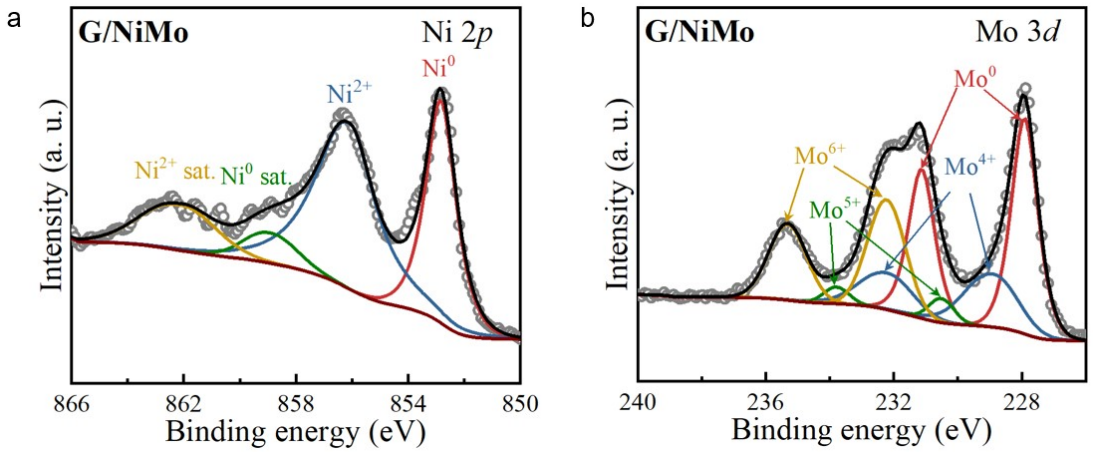

Figure S9. High-resolution XPS spectra of G/NiMo sample. (a) Ni 2*p* spectrum. (b) Mo 3*d* spectrum.

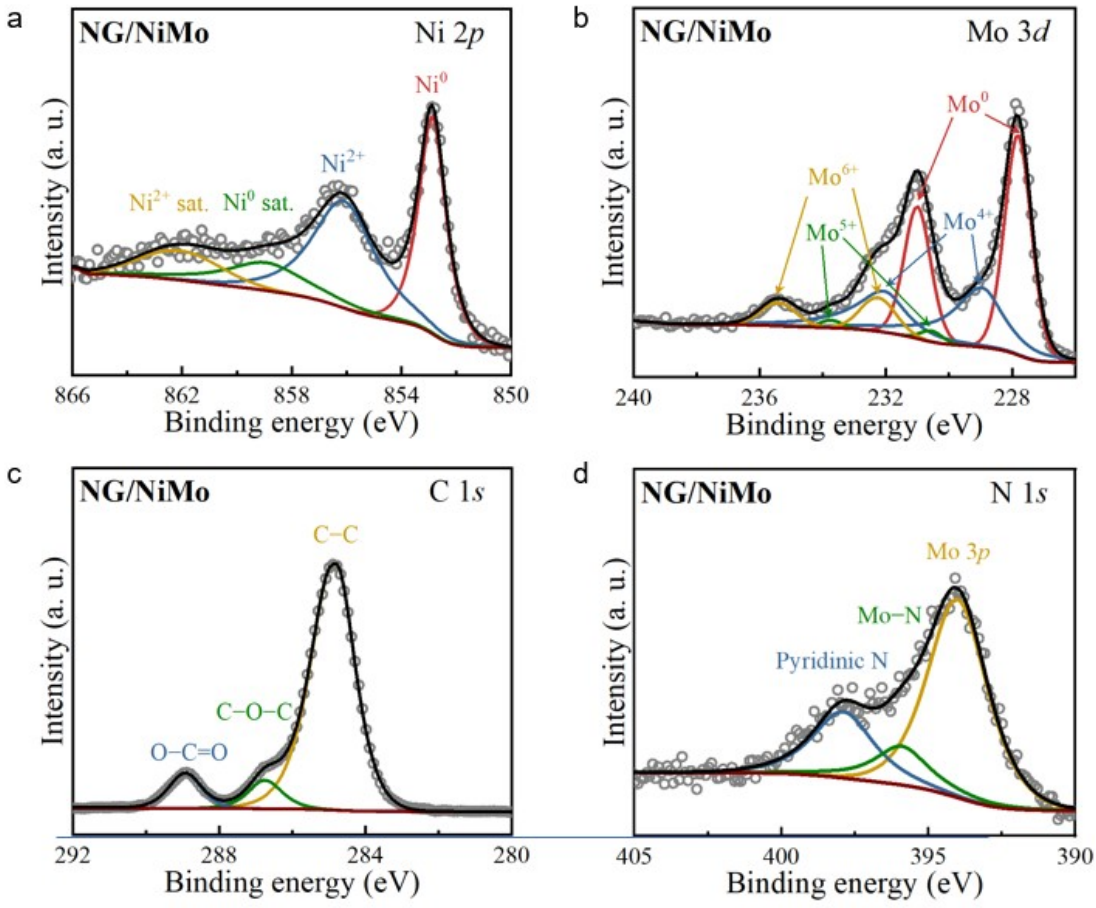

Figure S10. High-resolution XPS spectra of NG/NiMo sample. (a) Ni 2*p* spectrum. (b) Mo 3*d* spectrum. (c) C 1*s* spectrum. (d) N 1*s* spectrum.

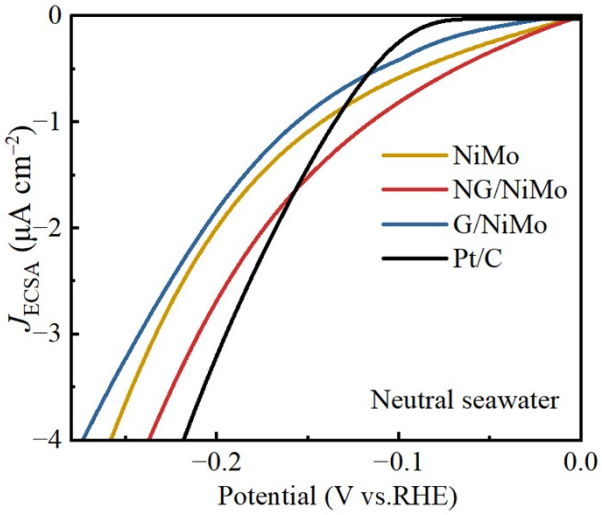

Figure S11. ECSA-normalized polarization curves of NiMo, NG/NiMo, G/NiMo, and commercial 20 wt% Pt/C in neutral seawater with 85% *iR* compensation.

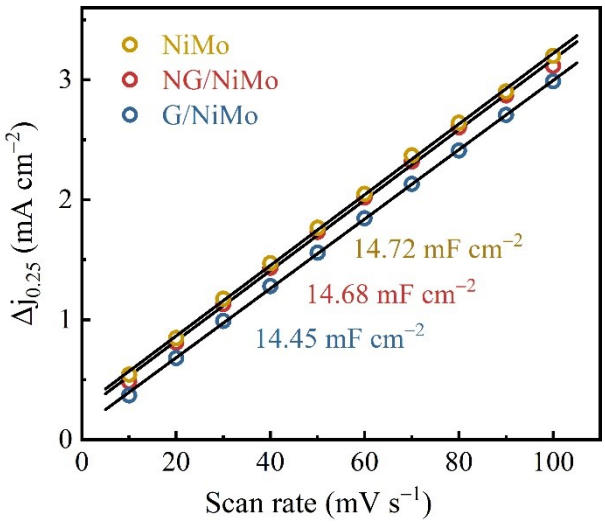

Figure S12. Capacitive current density plotted against scan rates for NiMo, NG/NiMo, and G/NiMo. The double-layer capacitance (C_{dl}) was determined from fitting these data.

The double-layer capacitance (C_{dl}) was determined from cyclic voltammetry (CV) tests to estimate the electrochemically active surface area (ECSA). The quite similar C_{dl}

values, ranging between 14.45 and 14.72 mF cm^{-2}, are measured for NiMo, NG/NiMo, and G/NiMo.

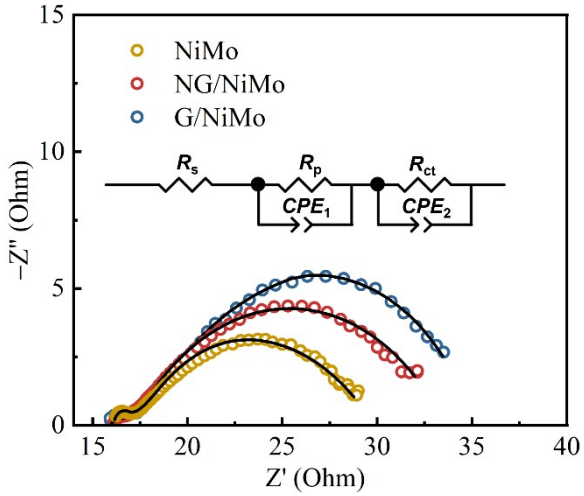

Figure S13. Electrochemical impedance spectra of NiMo, NG/NiMo, and G/NiMo. The black curves represent the fitting results. Inset: the corresponding equivalent circuit model.

R_s is the electrolyte resistance. R_p corresponds to the mass-transfer resistance of the adsorbed species at electrode surface. R_{ct} represents the charge-transfer resistance between the catalyst surface and electrolyte. The half-circles in the Nyquist plots were fitted to evaluate the R_{ct}. The R_{ct} values are measured as 11.32, 12.50, 13.85 Ω for NiMo, NG/NiMo, and G/NiMo, respectively.

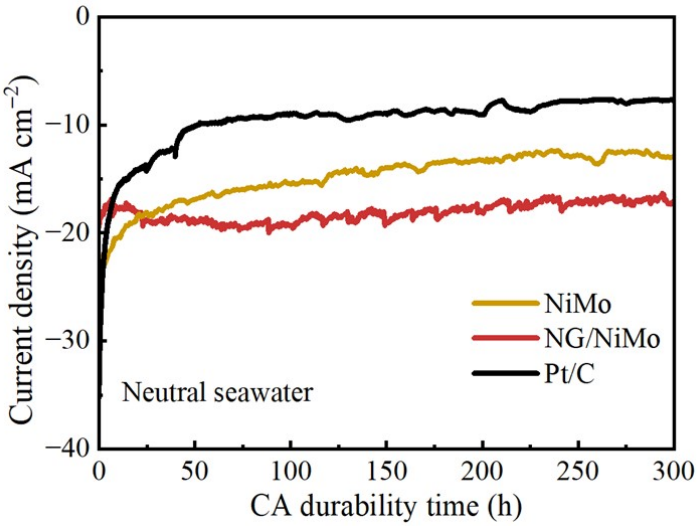

Figure S14. Chronoamperometry measurements of NiMo, NG/NiMo, and commercial 20 wt% Pt/C.

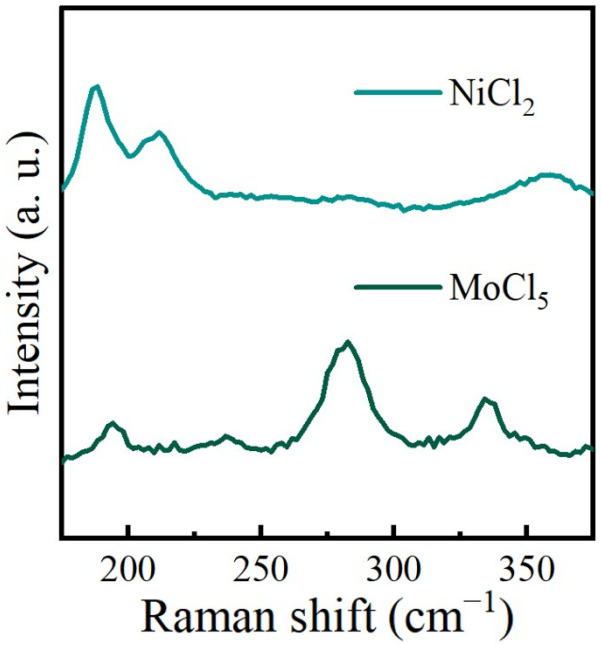

Figure S15. Raman spectra of standard $NiCl_2$ and $MoCl_5$ samples.

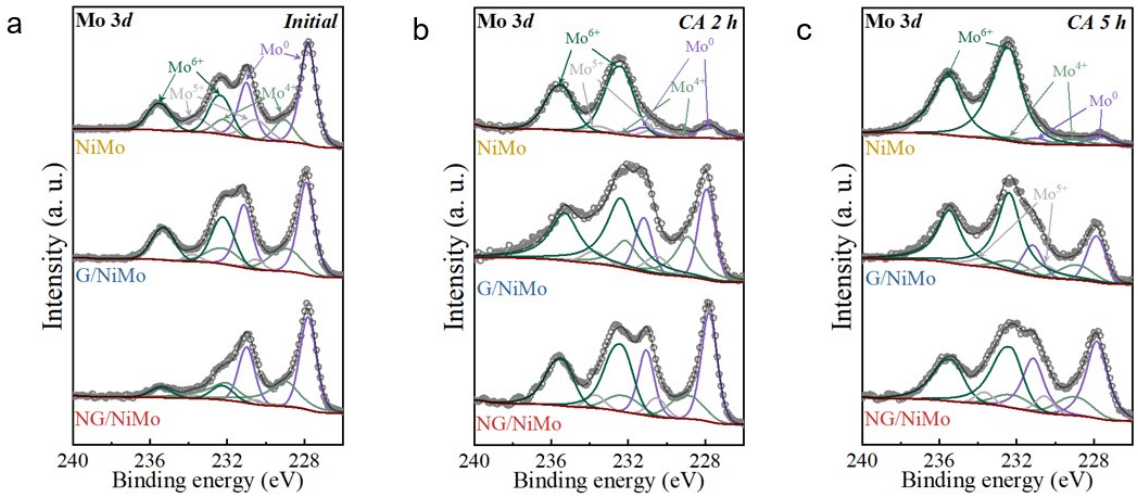

Figure S16. XPS Mo 3*d* spectra of NiMo, G/NiMo, and NG/NiMo. (a) Initial samples, and samples after (b) 2-h and (c) 5-h CA tests.

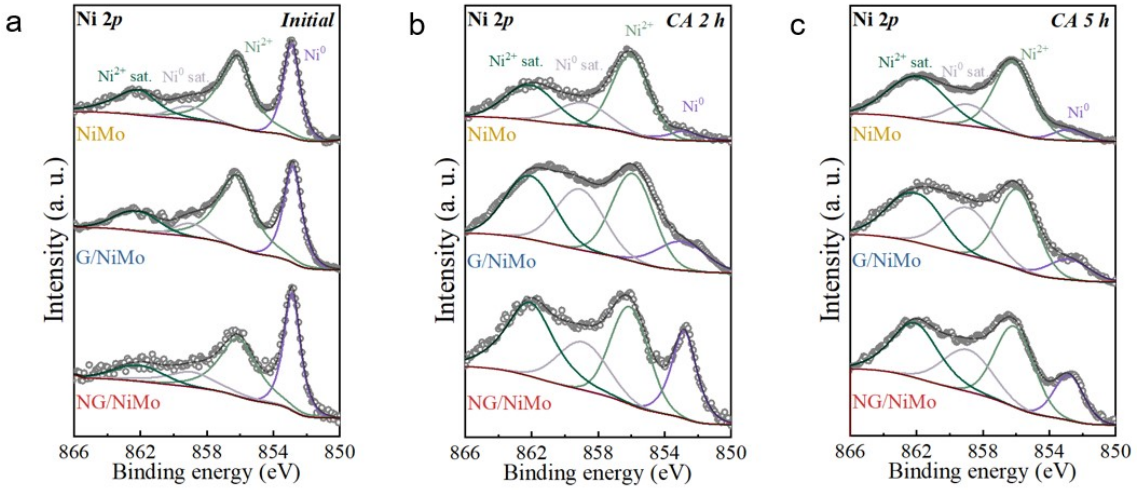

Figure S17. XPS Ni 2*p* spectra of NiMo, G/NiMo, and NG/NiMo. (a) Initial samples, and samples after (b) 2-h and (c) 5-h CA tests.

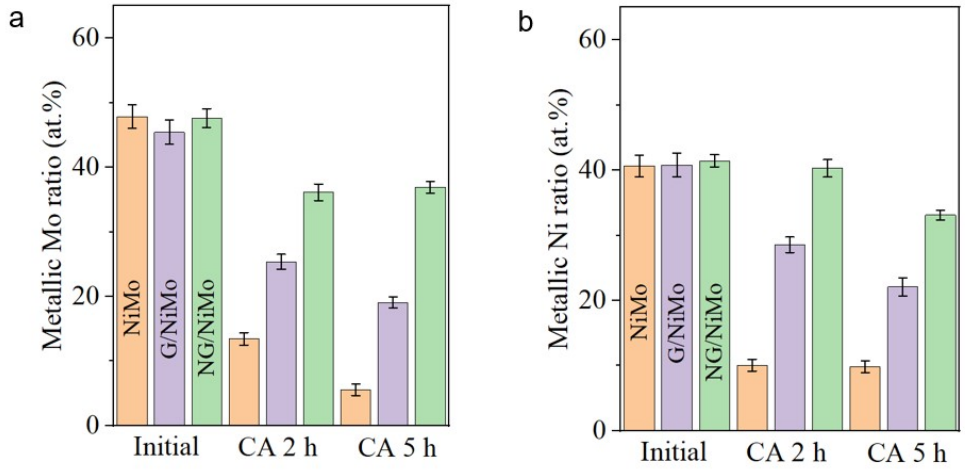

Figure S18. Metallic (a) Mo and (b) Ni ratios of NiMo, NG/NiMo, and G/NiMo during various CA durability times.

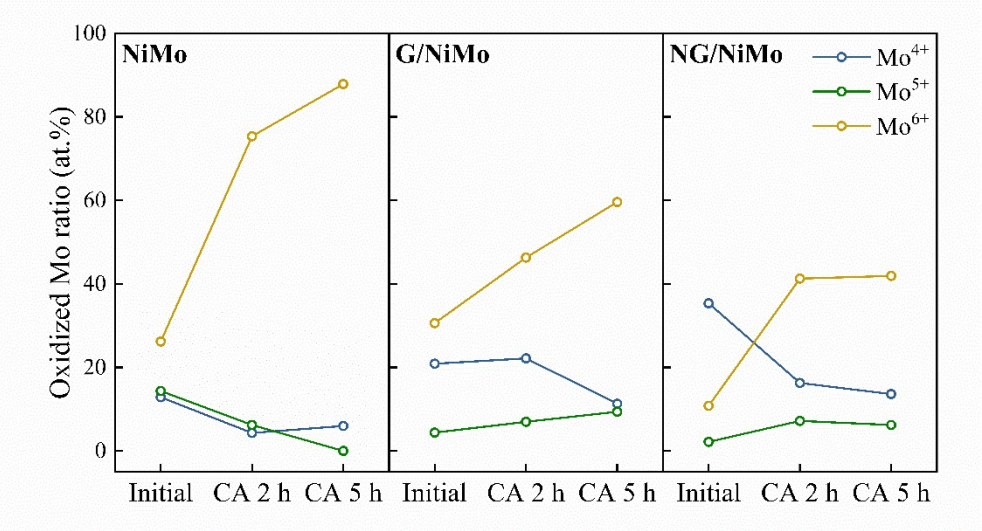

Figure S19. Comparisons of the oxidative Mo ratios of NiMo, NG/NiMo, and G/NiMo during various CA durability times.

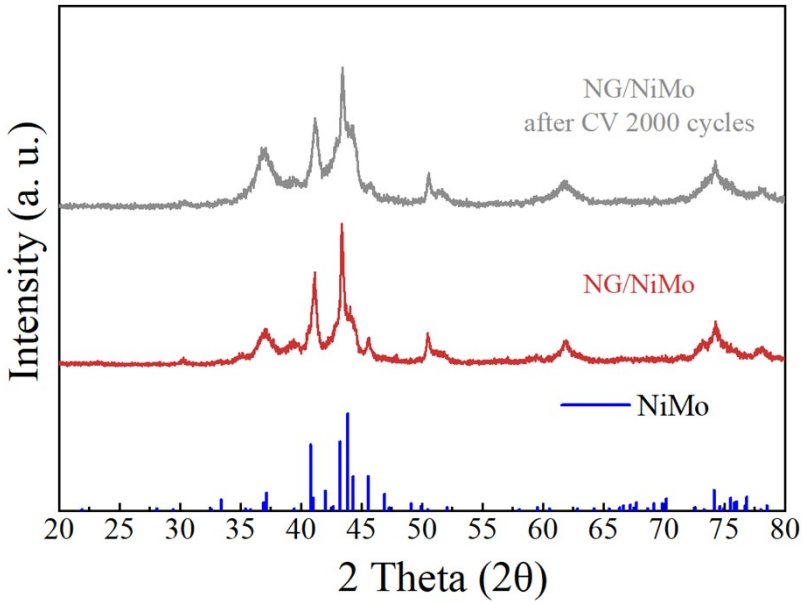

Figure S20. XRD pattern of NG/NiMo after 2000 CV cycles test.

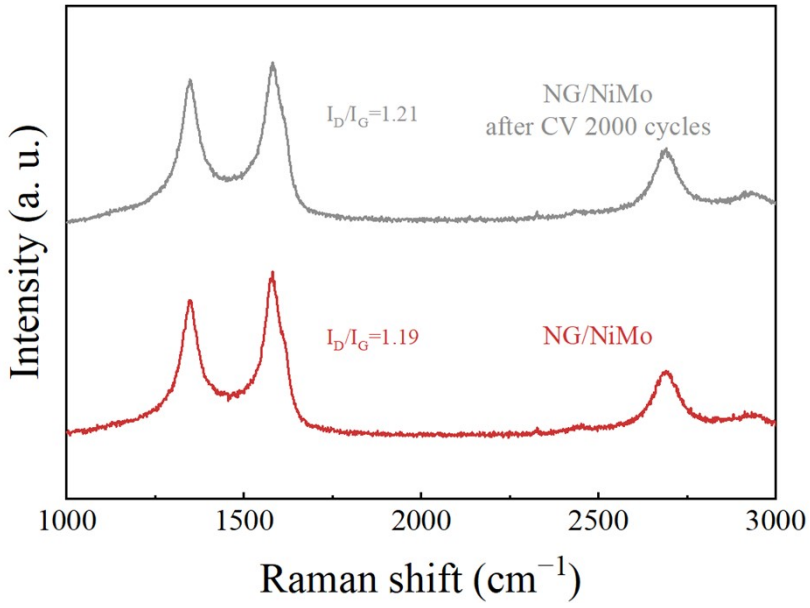

Figure S21. The Raman spectrum of NG/NiMo after 2000 CV cycles test.

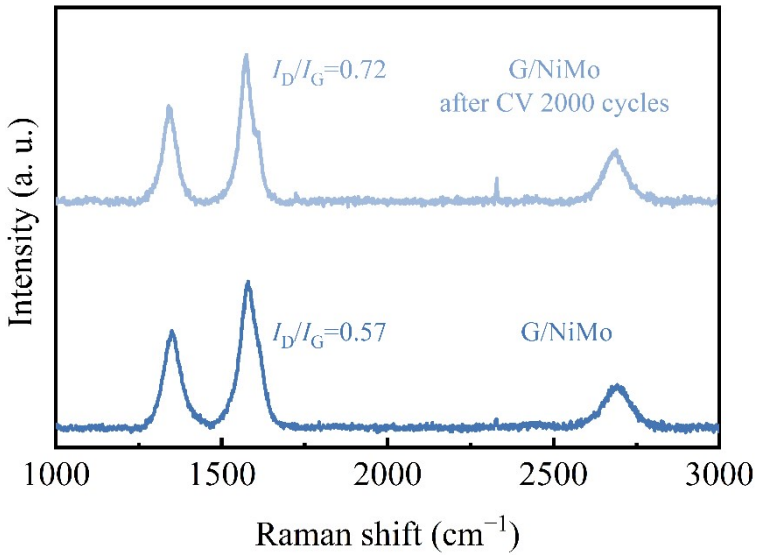

Figure S22. The Raman spectrum of G/NiMo after 2000 CV cycles test.

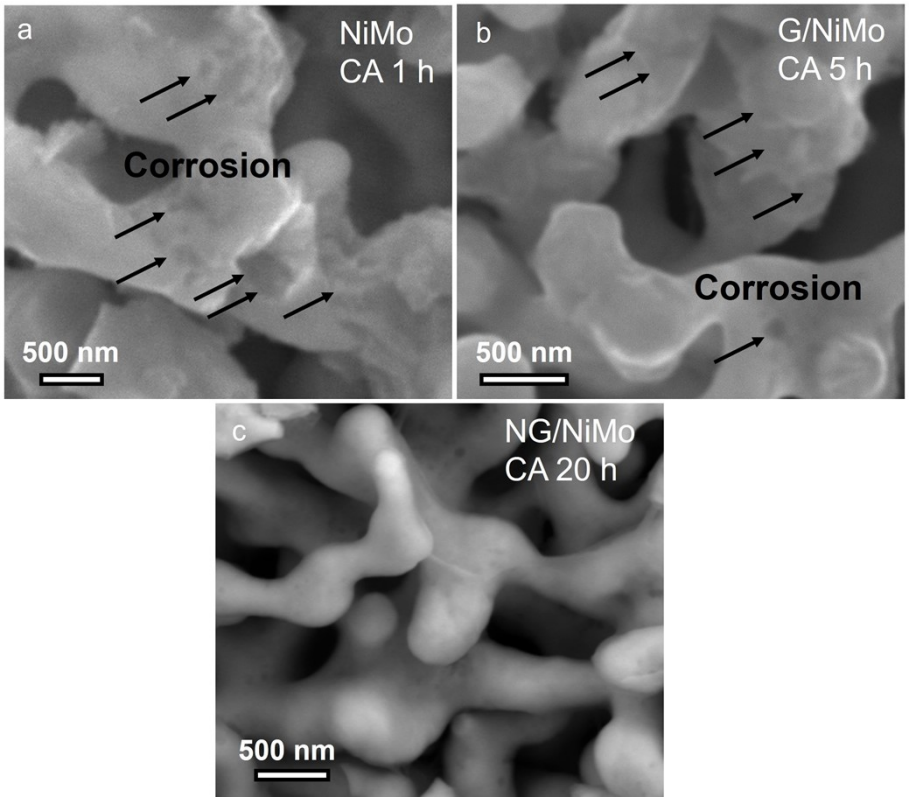

Figure S23. SEM images of (a) NiMo after a 1-h CA test, (b) G/NiMo after a 5-h CA test, and (c) NG/NiMo after a 20-h CA test.

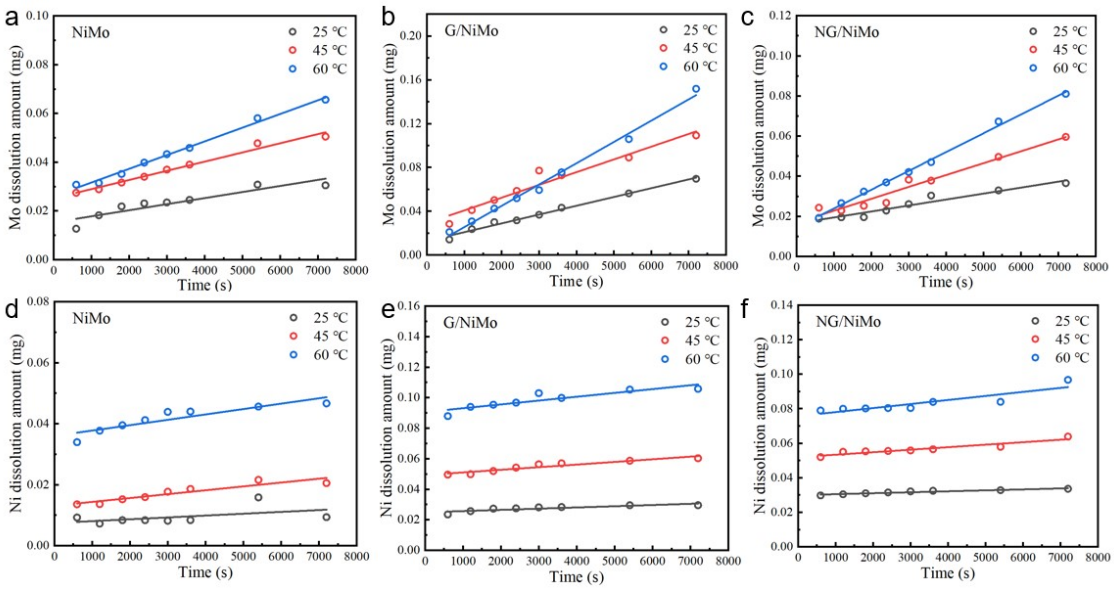

Figure S24. Metal dissolution amount plotted against time at different temperature. (a-c) Dissolved Mo amounts for NiMo, G/NiMo, and NG/NiMo. (d-f) Dissolved Ni amounts for NiMo, G/NiMo, and NG/NiMo.

Supporting tables

Table S1. MD LJ parameters for the Na^+, Cl^-, and H_2O with substrates.

\	ε (kcal mol^{-1})	σ (Å)	q (e)
Na^+	0.3526418	2.15953849	+1
Cl^-	0.0127850	4.83045285	−1
H	0	0	+0.4238
O	0.1553	3.166	−0.8476
Ni	11.98300	2.282000	0
Mo	0		
C (graphene)	19.320999	2.551000	0
C (linking to nitrogen)	0.081262	3.590000	0
N	0.083652	2.760000	+0.49
	0.169933	3.250000	−0.98

Table S2. The proportion of Ni and Mo valence states of NiMo samples before and after 2 h and 5 h CA test at the potential of −0.6 V vs. RHE.

Sample	Element	Valence state	Content (at%)
NiMo	Ni	0	27.47
		2+	45.13
		Sat.	27.40
	Mo	0	46.58
		4+	12.89
		5+	14.36
		6+	26.20
NiMo after 2 h CA	Ni	0	9.83
		2+	38.53
		Sat.	51.64
	Mo	0	17.55
		4+	5.30
		5+	16.03
		6+	61.13
NiMo after 5 h CA	Ni	0	5.66
		2+	47.08
		Sat.	47.26
	Mo	0	14.12
		4+	2.62
		5+	7.90
		6+	75.37

Table S3. The proportion of Ni and Mo valence states of G/NiMo samples before and after 2 h and 5 h CA test at the potential of −0.6 V vs. RHE.

Sample	Element	Valence state	Content (at%)
G/NiMo	Ni	0	31.22
		2+	47.78
		Sat.	21.00
	Mo	0	44.10
		4+	20.88
		5+	4.40
		6+	30.61
G/NiMo after 2 h CA	Ni	0	12.62
		2+	32.94
		Sat.	54.44
	Mo	0	24.56
		4+	22.16
		5+	6.97
		6+	46.31
G/NiMo after 5 h CA	Ni	0	9.21
		2+	34.41
		Sat.	56.38
	Mo	0	19.69
		4+	11.31
		5+	9.40
		6+	59.61

Table S4. The proportion of Ni and Mo valence states of NG/NiMo samples before and after 2 h and 5 h CA test at the potential of −0.6 V vs. RHE.

Sample	Element	Valence state	Content (at%)
NG/NiMo	Ni	0	34.60
		2+	38.88
		Sat.	26.52
	Mo	0	54.65
		4+	35.37
		5+	2.18
		6+	10.81
NG/NiMo after 2 h CA	Ni	0	19.30
		2+	29.76
		Sat.	50.94
	Mo	0	35.22
		4+	16.28
		5+	7.19
		6+	41.29
NG/NiMo after 5 h CA	Ni	0	14.76
		2+	33.52
		Sat.	51.72
	Mo	0	38.26
		4+	13.62
		5+	6.21
		6+	41.92

Table S5. Comparison of corrosion parameters of various reported electrocatalysts in seawater.

Catalyst	E_{corr} (V vs. SHE)	I_{corr} (mA cm^{-2})	Electrolyte	Reference
NG/NiMo	−0.22	0.19	Simulated seawater	This work
NiMo	−0.33	0.21	Simulated seawater	This work
G/NiMo	−0.25	0.23	Simulated seawater	This work
RuMoNi	−0.62	0.1	1.0 M KOH + 0.5 M NaCl	*Nature Communications*, **2023**, 14, 3607
Ni foam	−0.83	0.0398	1.0 M KOH + 0.5 M NaCl	*Nature Communications*, **2023**, 14, 3607
Fe-NiMoSe@C	−0.05	0.2	Natural seawater	*ACS Sustainable Chemistry & Engineering*, **2023**, 11, 15338-15349
NiMoSe	−0.1	0.631	Natural seawater	*ACS Sustainable Chemistry & Engineering*, **2023**, 11, 15338-15349
NF/(CoMo)0.85Se	−0.3	0.631	Alkaline simulated seawater	*ACS Catalyst*, **2023**, 13, 15360−15374
NF/(CoMo)0.85Se @FeOOH	−0.32	0.158	Alkaline simulated seawater	*ACS Catalyst*, **2023**, **13**, 15360−15374
NiFe-LDH	−0.875	0.398	Alkaline seawater	*Advanced Materials*, **2024**, 36, 2306062
NiFe-LDH@Ag	−0.825	0.0794	Alkaline seawater	*Advanced Materials*, **2024**, 36, 2306062

Table S6. Comparison of the performance of the electrolyzer catalyzed by various cathode catalysts.

Catalyst	Heat temperature	Cell voltage at 1 A cm^{-2} (V)	Current density of durability test (A cm^{-2})	Durability time (h)	Degradation rates (mV/h)	Reference
NG/NiMo	60 ℃	1.86	1	300	0.59 (100 h) 0.49 (300 h)	This work
Cr_2O_3-CoO_x	60 ℃	2.3	0.5	100	1.46 (100 h)	*ACS Energy Letters*, **2019**, 4, 933-942
$Co_{3-x}Pd_xO_4$	60 ℃	2.62	1	25	−	*Advanced Materials*, **2023**, 35, 2210057
Ni-$FeWO_4$ @WO_3	60 ℃	1.85	0.2	250	0.31 (250 h)	*Advanced Materials*, **2024**, 36, 2308925
Ni-$FeWO_4$	60 ℃	2.05	0.2	100	1.35 (100 h)	*Advanced Materials*, **2024**, 36, 2308925
Fe, P-$NiSe_2$	60 ℃	1.92	0.8	200	−	*Advanced Materials*, **2021**, 33, 2101425
NiFeP	80 ℃	1.9	0.5	24	−	*Nature Communications*, **2023**, 14, 3934

Reference

1. K. Hu, S. Jeong, M. Wakisaka, J.-i. Fujita and Y. Ito, *Metals*, 2018, **8**, 83.
2. S. Nagashima, T. Ikai, Y. Sasaki, T. Kawasaki, T. Hatanaka, H. Kato and K. Kishita, *Nano Letters*, 2019, **19**, 7000-7005.
3. I. S. Joung and T. E. Cheatham Iii, *Journal of Physical Chemistry B*, 2008, **112**, 9020-9041.
4. H. J. C. Berendsen, J. R. Grigera and T. P. Straatsma, *Journal of Physical Chemistry*, 1987, **91**, 6269-6271.
5. G. Hummer, J. C. Rasaiah and J. P. Noworyta, *Nature*, 2001, **414**, 188-190.
6. G. Lin, J. Manuel Perez-Aguilar and Z. Gu, *Journal of Molecular Liquids*, 2023, **383**, 122054.
7. H. Watanabe, *The Journal of Chemical Physics*, 2018, **149**, 154101.
8. A. P. Thompson, H. M. Aktulga, R. Berger, D. S. Bolintineanu, W. M. Brown, P. S. Crozier, P. J. in 't Veld, A. Kohlmeyer, S. G. Moore, T. D. Nguyen, R. Shan, M. J. Stevens, J. Tranchida, C.

Trott and S. J. Plimpton, *Computer Physics Communications*, 2022, **271**, 108171.
9. A. Stukowski, *Modelling and Simulation in Materials Science and Engineering*, 2010, **18**, 015012.
10. P. E. Blöchl, *Physical Review B*, 1994, **50**, 17953-17979.
11. J. P. Perdew, K. Burke and M. Ernzerhof, *Physical Review Letters*, 1996, **77**, 3865-3868.
12. S. Grimme, J. Antony, S. Ehrlich and H. Krieg, *Journal of Chemical Physics*, 2010, **132**, 154104.
13. S. Grimme, S. Ehrlich and L. Goerigk, *Journal of Computational Chemistry*, 2011, **32**, 1456-1465.
14. Y. Wang, C. Woodward, S. H. Zhou, Z. K. Liu and L. Q. Chen, *Scripta Materialia*, 2005, **52**, 17-20.
15. C. B. Shoemaker and D. P. Shoemaker, *Acta Crystallographica*, 1963, **16**, 997-1009.
16. J. Li, Y. Liu, H. Chen, Z. Zhang and X. Zou, *Advanced Functional Materials*, 2021, **31**, 2101820.